Experimental assessment of the capabilities and limitations of NaI(Tl) scintillation-based gamma ray spectrometry

Thomas Schanzer [a]

[a] *School of Physics, University of New South Wales, Sydney, Australia*

ABSTRACT: We present measurements of the gamma ray spectra of six radioisotopes using a thallium-doped sodium iodide scintillation detector. We first explain the appearances of the spectra and calibrate the detector to allow energy measurements. We then analyse the spectra to derive three key measures of detector performance: resolution, intrinsic width and full energy peak efficiency. We relate the values of these parameters and their dependence on gamma ray energy to the capabilities and fundamental limitations of scintillation detection.

1. Introduction

The decay of unstable nuclei may result in the release of excess energy in the form of high-energy photons known as gamma rays, created when the product nuclei transition from excited to lower-energy states. The gamma ray energies produced by a given radionuclide are precisely determined by the energies of the initial and final states and therefore take on a discrete spectrum that is unique to the radionuclide (L'Annunziata 2007, p. 191).

The uniqueness of the spectra makes gamma spectrometry an invaluable tool in many applications that require the analysis of radioactive samples of unknown isotopic composition. Mero (1960), for example, demonstrates that it may be used to determine the uranium or thorium content of natural ores in the mining industry. The *Lunar Prospector* orbiter, launched in 1998, carried a gamma ray spectrometer that it used to map the distribution of radionuclides on the Moon's surface in an effort to "improve our understanding of lunar formation and evolution" (Lawrence et al. 1998).

a. Gamma ray detection

We have noted that the spectrum of gamma rays emitted by a radionuclide is discrete. In order to detect the gamma rays and measure their energies, however, they must be made to interact with and deposit energy in matter. We will show that observed spectra therefore differ from emitted spectra; the interaction mechanisms must be understood in order to interpret them.

The first interaction mechanism in gamma ray detectors is Compton scattering, whereby a photon is deflected by a stationary electron. It may be shown that the kinetic energy imparted to an electron (mass m_e) by a photon of energy E, undergoing Compton scattering at an angle θ, is

$$E\frac{2\left(E/\left(m_ec^2\right)\right)\sin^2(\theta/2)}{1+2\left(E/\left(m_ec^2\right)\right)\sin^2(\theta/2)}.$$

The angle dependence of the energy thus deposited into the detector material produces a continuous distribution of energies in the measured spectrum, known as the *Compton continuum*. The continuum has a finite extent, terminating at the *Compton edge*

$$E_c = \frac{2E^2}{m_ec^2+2E}, \tag{1}$$

where $\theta = \pi$ (i.e., when the photon is scattered back along its direction of incidence) and the maximum possible energy is deposited into the detector.

The second interaction mechanism is the photoelectric effect, which involves the absorption of a gamma photon's energy by an electron, ejecting it from its host atom. The electron then comes to rest in the detector material, such that the entire photon energy is deposited. The photoelectric effect is dominant at low energies ($\lesssim 2\times10^2$ keV for the detector used in this work) but diminishes rapidly with increasing energy, leaving Compton scattering as the dominant process at higher energies (UNSW School of Physics n.d.).

Measurement of the deposited energy may be achieved by using a crystal doped with a *phosphor*, whose atoms radiate part of the deposited energy as light, as the detector material. The minute amounts of light emitted by the crystal (the *scintillator*) are then amplified by a photomultiplier tube. Incoming photons eject photoelectrons from a cathode, which are accelerated between a series of electrodes (*dynodes*) of increasing electric potential. At each dynode, each incoming electron ejects multiple secondary electrons, producing a charge cascade and an easily measurable voltage pulse at the final anode (Hamamatsu

Corresponding author: Thomas Schanzer, t.schanzer@student.unsw.edu.au
Word count: 3696 words

Photonics 2007, p. 13). Key to the energy measurement is the fact that the amplitude of the pulse is proportional to the energy deposited in the scintillator; this allows the instrument to be calibrated.

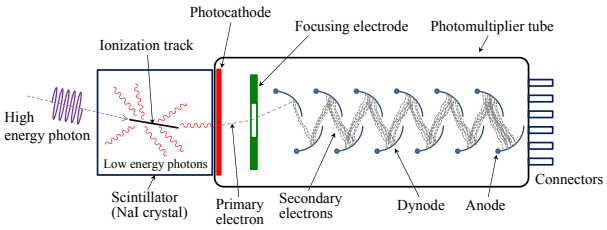

FIG. 1. Diagram of the scintillator and photomultiplier tube used to detect gamma photons. Adapted from Qwerty123uiop (2013) under the Creative Commons Attribution-Share Alike 3.0 Unported license.

b. Typical gamma ray spectra

The aforementioned interactions of the gamma photons with the detector, along with other interactions in the surrounding shielding (Crosthwaite n.d.) complicate the interpretation of the resulting spectra. A monochromatic source will not produce a single sharp peak, but rather a wider *full energy peak* or *photopeak* corresponding to photons whose entire energy is deposited in the detector and a lower-energy Compton continuum corresponding to incomplete energy transfer via Compton scattering.

Of particular interest is the width (FWHM), ΔE, of the full energy peak, which determines the resolving power of the spectrometer (i.e., its ability to distinguish two closely-spaced energies). If the cascading arrival of electrons at the anode of the photomultiplier tube is modelled as a Poisson process, with each arrival independent of the last, the amplitude of a voltage pulse (and the measured gamma ray energy) should have a standard deviation proportional to the square root of the average amplitude: $\Delta E \propto \sqrt{E}$. Basic manipulations then yield $(\Delta E/E)^2 = B/E$ for some constant B. In real detectors, however, the arrivals are not entirely independent, leading to the empirical expression

$$\left(\frac{\Delta E}{E}\right)^2 = \frac{B}{E} + W_I^2, \tag{2}$$

where the constant W_I is known as the *intrinsic width* of the detector (UNSW School of Physics n.d.). Observe that the resolution $\Delta E/E$ improves with increasing energy. In the limit as $E \to \infty$, W_I is the best resolution that may be achieved.

c. Overview

In § 2, we will describe the configuration and operation of the particular spectrometer used in this work and our approach to characterising the peaks in our spectra. § 3 will present the results of our measurements and their analysis, beginning by explaining the appearances of the spectra and then considering the calibration, resolution and full energy peak efficiency of the detector. § 4 will discuss the two primary limitations and sources of uncertainty in our experiment and propose solutions for implementation in future work.

2. Methods

The scintillator used in this work was a thallium-doped sodium iodide (NaI(Tl)) crystal, contained in a lead housing into which the radioisotope samples were lowered. The photomultiplier pulses were amplified, then digitised by a multi-channel analyser, allowing them to be sorted into 2048 amplitude bins of equal width, ideally corresponding to 2048 energy bins of equal width.

Six radioisotopes were tested: ^{241}Am, ^{133}Ba, ^{60}Co, ^{137}Cs, ^{152}Eu and ^{22}Na. For each radioisotope sample, counting was conducted for a known period of time and the resulting number of pulses in each of the 2048 bins was recorded. For a full description of the measurement setup and the instruments used, refer to the student notes (UNSW School of Physics n.d.).

The count data were analysed and visualised using Python 3.9. Two methods for extracting the locations and widths of peaks were used and evaluated. The first involved fitting a Lorentzian function of the form

$$y = \frac{a}{1 + \left(\frac{x - x_0}{\mathrm{FWHM}/2}\right)^2} + b \tag{3}$$

to the part of the spectrum in the immediate vicinity of each peak using ordinary least-squares regression. The uncertainty in the number of pulses, n, falling in a given amplitude bin was estimated by $\sqrt{n}$ in accordance with Poisson statistics (gamma ray arrivals are random, independent and steady over time), and this was passed as an argument to the fitting function. We thus obtained the height a, base b, location x_0 and FWHM of each peak.

The alternative was to use the pre-made peak finding routine `scipy.signal.find_peaks` in SciPy 1.7.3 (Virtanen et al. 2020). The routine takes the channel with the highest count as the centre of the peak; to reduce the influence of noise on this determination, the spectra were smoothed using a Gaussian filter with standard deviation $\sigma = 2$. It then draws a horizontal line through the top of each peak, using the points on the left and right where the line intersects the spectrum again (or else the endpoints of the dataset) to delineate a basin on each side of the peak. The higher of the lowest points in the left and right basins is taken to be the baseline. The width is then measured halfway between the baseline and maximum of the peak.

The advantages and disadvantages of the two methods are discussed in § 4, but since their results differed in places

and neither gave entirely satisfactory results, the final values for the peak parameters were found by averaging the outputs of the Lorentzian fit and the `find_peaks` routine (with Gaussian pre-smoothing of the spectra). The locations of the maxima prior to Gaussian smoothing were also included. The uncertainties were taken to be half the range of these values, with a minimum uncertainty of one channel imposed to eliminate unrealistic values.

3. Results

a. The spectra and their features

Figure 2 shows the six spectra that were obtained. It is reassuring that they are qualitatively similar to published spectra from similar NaI(Tl) detectors (e.g., Bee Research Pty. Ltd. (n.d.)). We were able to match the peaks to their corresponding gamma ray energies by comparing the measured spectra and peak locations to those given by Heath (1974) (for gamma rays) and Shirley and Lederer (1978) (for X-rays). We will now examine each spectrum in detail, explaining the features that are present. The explanations are partly drawn from the gamma spectrum database of Bee Research Pty. Ltd. (n.d.), the radioactive source list of LD Didactic (n.d.) and the decay schemes of Shirley and Lederer (1978).

1) Americium-241

^{241}Am undergoes alpha decay to ^{237}Np. 85% of the product nuclei initially exist in an excited state and then fall into the ground state, emitting a 59.537 keV gamma photon. This manifests as a peak near channel 50 in our spectrum. The excited nucleus may also fall to the first excited state instead of the ground state, emitting a 26.345 keV gamma photon; this is the source of the peak at channel 17. Almost no signal is seen in the remainder of the spectrum.

2) Barium-133

^{133}Ba decays via electron capture to ^{133}Cs, whose nuclei may initially exist in a number of excited states. The decay of these excited states gives rise to the four highest-energy peaks in the spectrum. The lowest-energy peak corresponds not to a gamma ray, but a characteristic X-ray of Cs. The X-ray is produced by *internal conversion*, where the excited nucleus transfers its energy to one of its inner-shell electrons, ejecting it from the atom instead of producing a gamma ray. A remaining electron fills the inner-shell vacancy, emitting the X-ray photon.

3) Cobalt-60

^{60}Co undergoes beta decay to excited states of ^{60}Ni, producing the two photopeaks observed at the right end of the spectrum. Compton scattering of these gamma photons in the detector produces a long Compton continuum that spans several hundred channels, terminating at the Compton edge near channel 900. At the left end of the continuum (near channel 200), a wide, skewed peak is observed. This is a *backscatter* peak, created by gamma rays that undergo Compton scattering in the lead shielding surrounding the detector and are redirected into the detector with lower energies. Finally, the narrow leftmost peak corresponds to a characteristic X-ray of lead; the high-energy ^{60}Co gamma rays eject inner-shell electrons in the detector's lead shielding via the photoelectric effect and remaining electrons fill the vacancy, emitting X-ray photons.

4) Caesium-137

^{137}Cs undergoes beta decay to ^{137}Ba, 95% of whose nuclei initially exist in an excited state that decays, emitting a 661.638 keV gamma photon and producing the single photopeak at the right end of the spectrum. The corresponding Compton continuum and backscatter peak are seen in the middle of the spectrum, with characteristic X-rays of barium (produced by internal conversion as previously explained) and the lead housing at the low-energy end.

5) Europium-152

^{152}Eu decays via electron capture and positron emission to ^{152}Sm, which has many possible excited states. This produces seven visible gamma ray peaks in the spectrum. Characteristic X-rays of samarium (from internal conversion) and the lead housing are also observed.

6) Sodium-22

^{22}Na decays via electron capture and positron emission to ^{22}Ne, primarily into an excited state that emits a 1274.511 keV gamma photon when it transitions to the ground state. This produces the rightmost photopeak and Compton continuum in the spectrum. Additionally, the positrons produced directly by the decay of ^{22}Na annihilate with electrons in the surrounding material, each pair emitting two 511.005 keV gamma photons in opposite directions. This gives rise to the photopeak near channel 470 and the corresponding Compton continuum. Characteristic X-rays of the lead housing are observed.

b. Spectrometer calibration

It was mentioned in § 1 that the energy deposited into the detector should be proportional to the amplitude of the voltage pulse sent to the multi-channel analyser (and thus to the channel number assigned to the pulse). We now seek to calibrate the spectrometer: determine the constant of proportionality and use it to formulate a relationship between channel number and energy. This step is essential in every application of gamma ray spectrometry; the spectra are useless without corresponding energy scales.

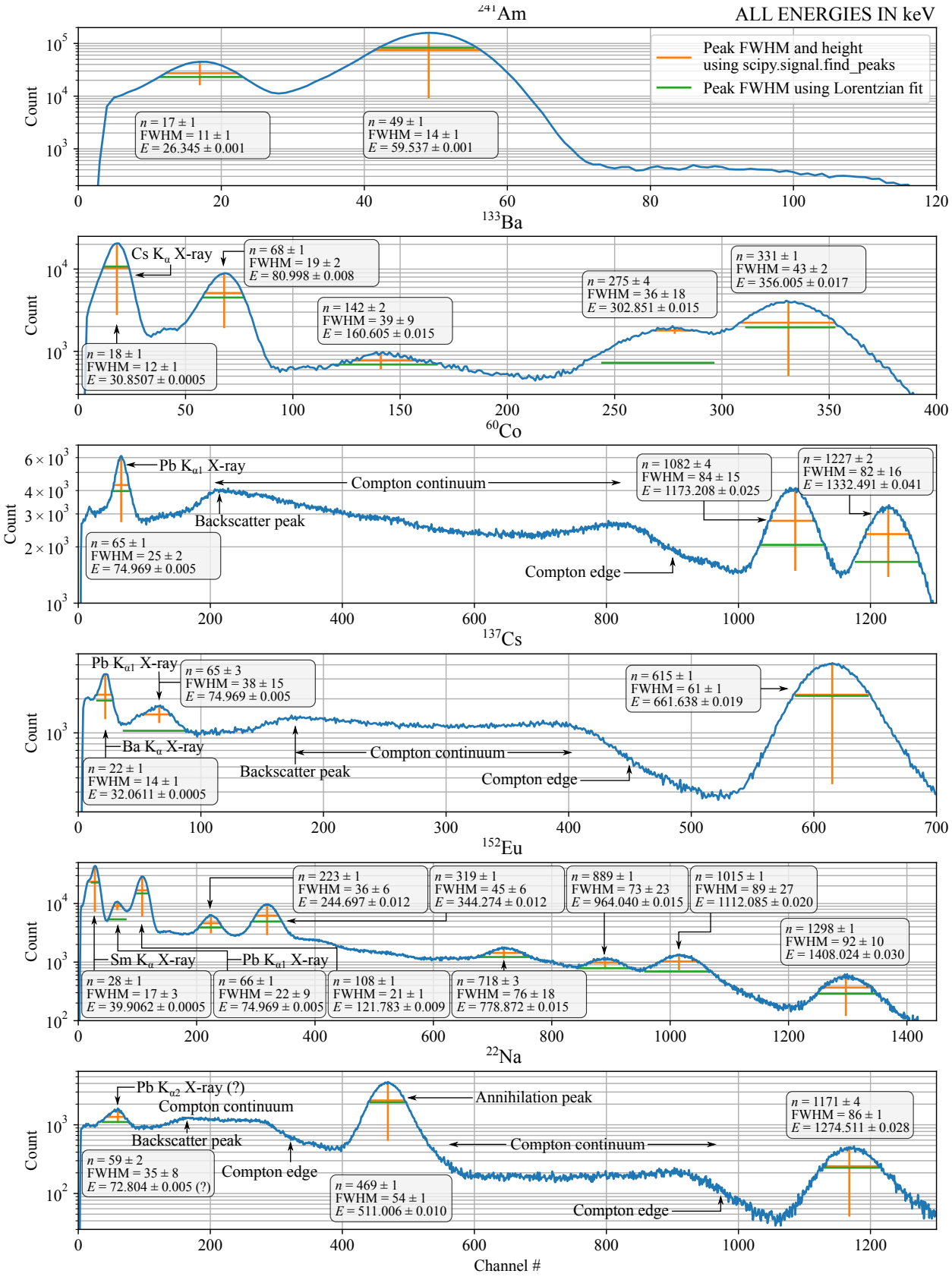

FIG. 2. Gamma ray spectra of the six radioisotopes tested. Each peak is annotated with the channel number n of its centre, its full width at half maximum and the accepted value E for its energy in keV (derived from Heath (1974) for gamma rays and Shirley and Lederer (1978) for X-rays). Orange vertical and horizontal lines extend from base to top and across each peak at the half-maximum height, as determined by the `scipy.signal.find_peaks` routine. Green horizontal lines span the peaks at half-maximum height, as determined by Lorentzian curve fitting.

Our approach is to choose nine well-resolved peaks that (roughly) evenly span the observed energy range and have good Lorentzian fits (1408, 1275, 779, 662, 511, 344, 245, 122 and 59.5 keV) to generate the calibration parameters, and use the remaining peaks to assess the accuracy of the calibration by comparing their accepted energies to the energies implied by the calibration parameters.

The measured centres of the peaks and uncertainties (obtained according to the method in § 2) and corresponding accepted energies and uncertainties (from Heath (1974)) were collated. A linear orthogonal distance regression of energy against peak centre was performed, yielding the relationship

$$E = [(1.080 \pm 0.003)n + (3.3 \pm 1.9)]\text{keV} \qquad (4)$$

where n is the channel number. Figure 3 reveals that energy is indeed a linear function of channel number; the coefficient of determination of the fit is $R^2 = 1 - 5.8 \times 10^{-5}$ and the residuals are on the order of 1%.

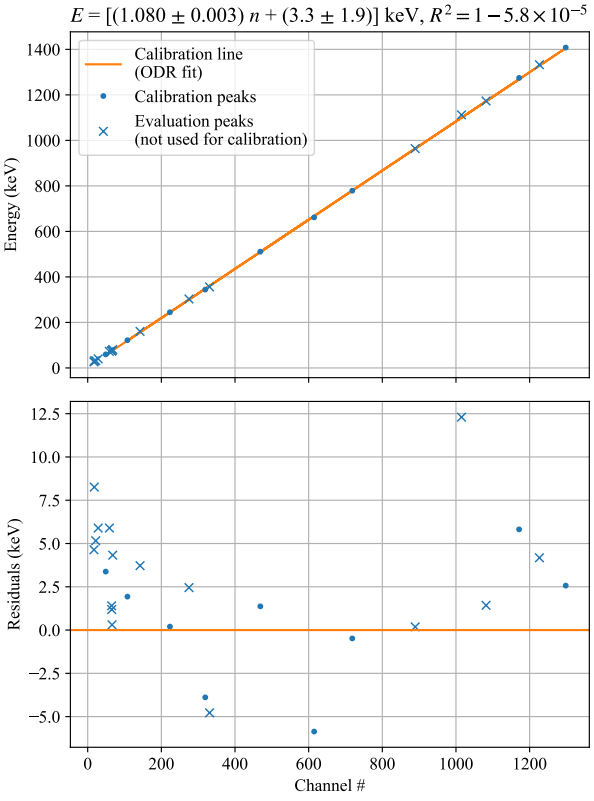

FIG. 3. Top: plot of peak locations against accepted energy values, with linear ODR fit in orange. Uncertainties are too small to be displayed. Bottom: residuals of the fit in the top plot, corresponding to the error between the energy predicted from the experimental calibration and the accepted energy value.

Estimates for the remaining peak energies, generated using 4, are displayed in Table 1. Seven out of sixteen predictions were consistent with the accepted values given the prediction uncertainty, with an average error (predicted minus accepted) of -1.4σ. The inconsistency of some of the predictions could be due to underestimation of the uncertainty in the central channel of particularly skewed or noisy peaks, the superposition of the peaks upon other spectral features (or other unresolved peaks) or misidentification of the accepted energies (though this is unlikely). The fact that almost all the energies were under-predicted suggests that the set of nine chosen calibration peaks may not have been representative of the remaining peaks. This hypothesis is supported by the fact that most of the inconsistent peaks have energies below 100 keV and lie at the extreme lower end of the calibration set. Future work should test the dependence of the errors on the choice of calibration set.

Isotope	**Accepted energy (keV)**	**Predicted energy (keV)**	**Error (predicted minus accepted)**
^{133}Ba	30.851 ± 0.001	22.6 ± 1.9	-4.2σ
^{133}Ba	80.998 ± 0.008	76.7 ± 2.1	-2.1σ
^{133}Ba	160.605 ± 0.015	156.9 ± 2.4	-1.6σ
^{133}Ba	302.851 ± 0.015	300.4 ± 2.8	-0.9σ
^{133}Ba	356.005 ± 0.017	360.8 ± 3.0	1.6σ
^{137}Cs	32.061 ± 0.001	26.9 ± 2.0	-2.6σ
^{137}Cs	74.969 ± 0.005	73.8 ± 2.1	-0.6σ
^{137}Cs	661.638 ± 0.019	—	—
^{152}Eu	39.906 ± 0.001	34.0 ± 2.0	-3.0σ
^{152}Eu	74.969 ± 0.005	74.7 ± 2.1	-0.1σ
^{152}Eu	121.783 ± 0.009	—	—
^{152}Eu	244.697 ± 0.012	—	—
^{152}Eu	344.274 ± 0.012	—	—
^{152}Eu	778.872 ± 0.015	—	—
^{152}Eu	964.040 ± 0.015	963.9 ± 4.8	-0.0σ
^{152}Eu	1112.085 ± 0.020	1099.8 ± 5.3	-2.3σ
^{152}Eu	1408.024 ± 0.030	—	—
^{22}Na	72.804 ± 0.005	66.9 ± 2.1	-2.8σ
^{22}Na	511.006 ± 0.010	—	—
^{22}Na	1274.511 ± 0.028	—	—
^{241}Am	26.345 ± 0.001	21.7 ± 1.9	-2.4σ
^{241}Am	59.537 ± 0.001	—	—
^{60}Co	74.969 ± 0.005	73.6 ± 2.1	-0.7σ
^{60}Co	1173.208 ± 0.025	1171.8 ± 5.5	-0.3σ
^{60}Co	1332.491 ± 0.041	1328.3 ± 6.0	-0.7σ

TABLE 1. Accepted values for the energies of the peaks in Figure 2, the corresponding predictions using the calibration equation (4) and the errors as fractions of the prediction uncertainties. Of course, the energies of the peaks that were used to generate the calibration cannot be predicted using the same calibration, and are left blank.

c. Energy resolution and intrinsic width

It is evident from Figure 2 that the limited resolution of the spectrometer has an impact on the results. For example, the 302.851 keV and 356.005 keV peaks of ^{133}Ba are barely resolved, and the 39.9062 keV peak of ^{152}Eu appears to be the superposition of two unresolved peaks.

We will now quantitatively analyse the spectrometer's resolving power. (2) suggests that a plot of $(\Delta E/E)^2$ against $1/E$ should yield a linear relationship with slope B and intercept W_I^2. Figure 4, using the FWHM data shown in Figure 2 and the accepted energies in Table 1, does indeed support this hypothesis. While there are two notable outliers, it is reassuring that the uncertainties we have derived for $(\Delta E/E)^2$ generally overlap with the regression line; this indicates that our derivation was reasonable. The magnitude of the uncertainty results from the ambiguity of the FWHM for asymmetric peaks, which we will discuss in more detail in § 4.

An ordinary least squares[1] regression of $(\Delta E/E)^2$ against $1/E$ yields an intrinsic width $W_I = 0.035 \pm 0.004$ for our detector. The fact that this is clearly nonzero is consistent with the findings of Zerby et al. (1961), who observed an "intrinsic line broadening" in Monte Carlo simulations of NaI(Tl) gamma ray spectrometers.

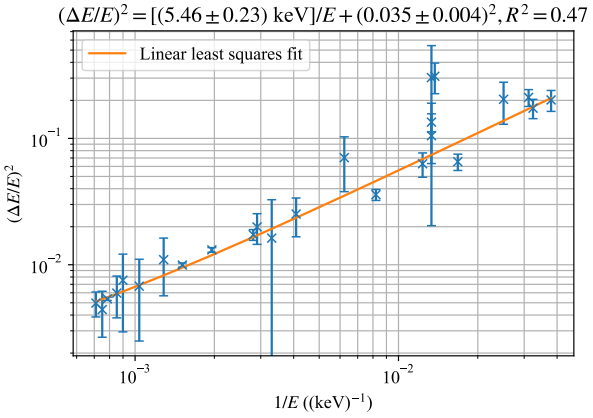

FIG. 4. Plot of $(\Delta E/E)^2$ against $1/E$, with a linear fit yielding an intrinsic width $W_I = 0.035 \pm 0.004$. A log-log scale is used instead of a linear one so that the datapoints in the lower left corner are clearly distinguishable. The uncertainty in $1/E$ is negligible compared to the uncertainty in $(\Delta E/E)^2$.

d. Full energy peak efficiency

The detector's full energy peak efficiency (hereafter FEPE) is the fraction of gamma photons produced at a given energy by the source that are counted in the spectrum's corresponding full energy peak. Eight full energy peaks (as in § b, well-resolved peaks that (roughly) evenly span the observed energy range) were chosen for analysis: 1408, 1275, 662, 511, 344, 245, 122 and 59.5 keV.

The net count rates for the peaks were determined by summing the counts in each peak's constituent channels, subtracting the contribution of the counts below the baseline level of the peak and dividing by the count time. The horizontal extent of each peak was determined subjectively rather than programmatically to ensure that the choices were reasonable. This naturally introduced undesirable uncertainties in the count sums; their magnitude was estimated by re-calculating the sums after extending all the windows by 10% (a value chosen arbitrarily but based on the expected level of uncertainty) in both directions, and then after contracting all the windows by the same amount. The uncertainty was taken to be half of the difference between the extended and contracted values.

The rate of corresponding gamma photon emission for each peak was determined by multiplying the total activity of the appropriate radioisotope sample (computed from the activity of the sample on its manufacturing date and the length of time since manufacturing) by the known relative gamma ray intensity at that energy (obtained from UNSW School of Physics (n.d.)). Dividing the net count rate by the rate of gamma photon emission yielded the FEPE, shown as a function of energy in Figure 5. As a first approximation, we neglect uncertainties in peak height and sample activity compared to the aforementioned uncertainties due to subjective choice of peak extent.

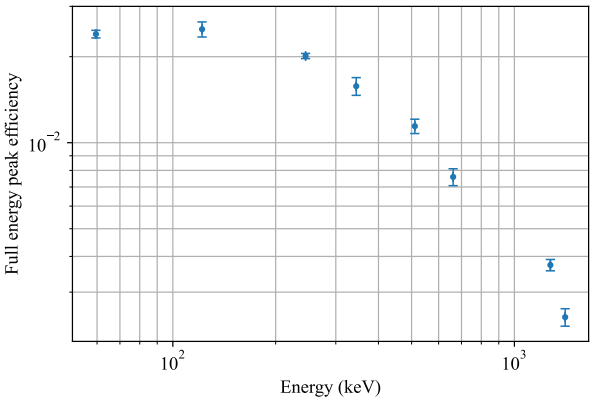

FIG. 5. Plot of net FEPE against peak energy. The uncertainty in energy is negligible.

We observe a FEPE that is approximately constant at energies below 2×10^2 keV but decreases roughly exponentially with increasing energy beyond this point. In fact, M. El-Khatib et al. (2016) devised a theoretical scheme for predicting the FEPE of a NaI(Tl) gamma spectrometer. While the details of the scheme and its derivation are highly non-trivial and entirely beyond the scope of this paper, we may at least qualitatively compare our results to theirs. They presented calculations for a wide range of detector geometries and positions; in Figure 6, we reproduce their Figure 6, which concerns the FEPE as a function of energy for one particular detector and position (the others are qualitatively similar, having the same decline in efficiency). Remarkably, this bears an extremely close resemblance to our Figure 5; even the numerical values are

[1] The uncertainties in the accepted energies E are negligible compared to the uncertainties in the FWHMs ΔE, justifying the use of ordinary least squares instead of orthogonal distance regression.

similar. This is strong evidence that our approach to measuring FEPE is valid and reasonably accurate. Future work could attempt a more quantitative comparison by applying the theoretical scheme to our detector.

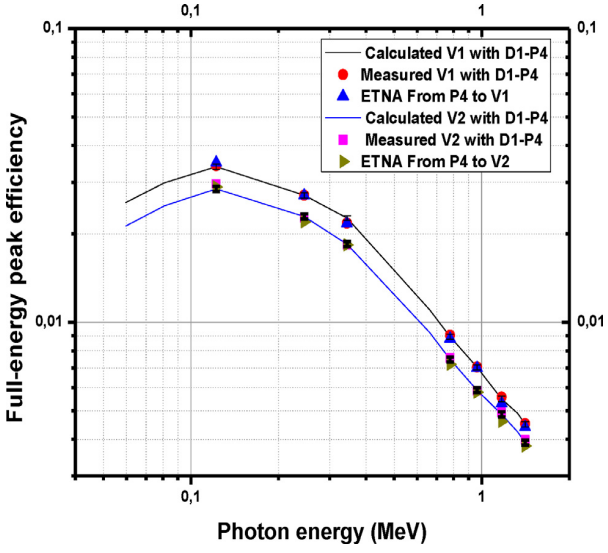

FIG. 6. Reproduction of Figure 6 in the paper by M. El-Khatib et al. (2016), showing the calculated theoretical efficiencies for two radioactive sources ("V1" and "V2") as solid lines. These are consistent with measured values (red dots and pink squares). Note the extremely close resemblance to Figure 5.

4. Discussion

We shall now discuss the factors that influenced the quality of our results and measures that may be taken in future work to mitigate them.

a. Determining peak location and FWHM

§ 2 alluded to difficulties in characterising the peaks in our gamma ray spectra in justifying the final approach used; we now extend this discussion. The method of Lorentzian curve fitting has several disadvantages, including

- The fact that the peaks may not be Lorentzian at all, as evidenced by decreases in fit quality when the subsets of the spectra considered "part of the peaks" were expanded (reducing the validity),
- The superposition of the peaks upon other spectral features (such as other peaks and their Compton continua), skewing them from the assumed Lorentzian shape, which must be symmetrical for an accurate fit,
- Ambiguity in the base levels of the peaks (the parameter b in (3), which was determined by the fitting routine with the sole aim of reducing mean squared error, neglecting physical considerations (before the addition of constraints, the calculated base level was often negative),
- The consequent ambiguity in the FWHM due to ambiguity in the base level, and
- Impossibly small reported uncertainties in the fit parameters (much less than one channel in peak location and FWHM), which were simply incompatible with the observed fit quality.

After observing the above limitations, the `scipy.signal.find_peaks` routine, whose operation is explained in § 2, was chosen because it is able to characterise the peaks while making far weaker assumptions about their shape. In particular, the routine's approach to determining the baseline level of a peak is, physically, much more reasonable. The reported FWHM value also corresponds to the literal width of the peak at some height, rather than an inferred width from a fit that may deviate from the true peak shape. Nonetheless, the routine also has its limitations, including

- The fact that it simply takes the location and height of the highest data point as the location and height of the peak, and similarly for the base and FWHM measurements, increasing the impact of random noise compared to curve fitting (which recognises a distribution of data points about the fitted curve), and
- Its inability to natively estimate the uncertainties in the peak parameters, forcing an *ad hoc* solution based partly in estimation and human judgement rather than mathematics.

We have used the discrepancy between the two approaches to our advantage. The Lorentzian method usually underestimated the peaks' base levels and overestimated their FWHMs, while the SciPy routine may have done the opposite, overestimating the base levels by choosing the higher of the minima to the left and right of each peak. This is evidenced by the fact that the green horizontal Lorentzian half-maximum lines in Figure 2 invariably lie lower than the yellow half-maximum lines from the SciPy routine. We therefore conjectured that the true half-maximum level should lie between these two estimates, leading us to our final values and uncertainties.

Future work should further investigate the methods of peak characterisation used in modern-day research and evaluate their performance.

b. Resolution limits

The limited resolving power of the detector, as investigated in § c, is an inherent feature of the family of scintillation detectors, of which our NaI(Tl) detector is a member. Another approach to gamma ray detection uses semiconductors, whose electrons may be excited from the valence

band to the conduction band by incoming gamma photons. The arrival of gamma photons thus increases the conductivity of the semiconductor, which may be measured electrically. Semiconductor detectors have far better resolving power than scintillators, but must be kept at cryogenic temperatures, making them infeasible for future work in the teaching laboratory. Comparison of our spectra to those of Heath (1974), who used silicon and germanium semiconductor detectors, clearly shows that we were only able to observe a small subset of the many gamma energies present.

5. Conclusion

We have successfully acquired the gamma ray spectra of six radioisotope samples using a NaI(Tl) scintillation detector and shown that the theory governing the fundamental processes occurring in the source and detector justifies their appearance.

We calibrated the spectrometer and assessed the accuracy of energies predicted using the calibration, finding that although some of the predictions were consistent with expectations, others were not due to other uncertainty sources, the superposition of peaks on other spectral features or misidentification of peaks with accepted energy values.

We then calculated the detector's resolution, which improved with increasing gamma ray energy, and calculated its intrinsic width, the fundamental limit on its resolution. The existence of this fundamental limit is consistent with the behaviour expected for NaI(Tl) detectors based on computer models.

Finally, we calculated the full energy peak efficiency of the detector as a function of energy and demonstrated a remarkable agreement between our results and theoretical values.

In summary, we have demonstrated the utility of scintillation-based gamma ray spectrometry, as well as its limitations. Our findings will be useful in the design of future investigations into gamma spectrometry.

Acknowledgments. The author gratefully acknowledges the assistance of the UNSW School of Physics, which provided the facilities and equipment for this work, the staff in the UNSW Higher Year Physics Laboratory, who provided guidance during the experiment, and his laboratory partner Oscar Prien, with whom he had enlightening discussions.

Data availability statement. The raw data and Python code used to produce the results in this report are available as supplementary material at `https://github.com/tschanzer`. They are also available from the author upon request.

References

Bee Research Pty. Ltd., n.d.: Gamma spectrum database. URL https://www.gammaspectacular.com/blue/gamma_spectra, accessed 28/03/22.

Crosthwaite, M. H., n.d.: Review of the gamma spectrum structure. URL http://www.people.vcu.edu/~mhcrosthwait/clrs322/ReviewoftheGammaSpectrum.htm, accessed 28/03/22.

Hamamatsu Photonics, 2007: *Photomultiplier tubes: basics and applications*. 3rd ed., Hamamatsu Photonics K. K.

Heath, R. L., 1974: Gamma-ray spectrum catalogue: Ge(Li) and Si(Li) spectrometry. Tech. rep., Aerojet Nuclear Company, Idaho Falls, Idaho. URL https://www.osti.gov/biblio/4244626.

L'Annunziata, M. F., 2007: *Radioactivity : introduction and history*. 1st ed., Elsevier, Amsterdam.

Lawrence, D. J., W. C. Feldman, B. L. Barraclough, A. B. Binder, R. C. Elphic, S. Maurice, and D. R. Thomsen, 1998: Global elemental maps of the moon: The lunar prospector gamma-ray spectrometer. *Science*, **281 (5382)**, 1484–1489, https://doi.org/10.1126/science.281.5382.1484.

LD Didactic, n.d.: Radioactive sources. URL https://www.ld-didactic.de/software/524221en/Content/Appendix/RadioactiveSources.htm, database of radioactive source information and gamma ray spectra, accessed 12/04/22.

M. El-Khatib, A., M. M. Gouda, M. S. Badawi, A. Hamzawy, N. S. Hussien, and M. I. Abbas, 2016: Calculation of the full-energy peak efficiency of nai(tl) detector using the efficiency transfer method for large radioactive cylindrical sources. *Chinese Journal of Physics*, **54 (4)**, 592–606, https://doi.org/https://doi.org/10.1016/j.cjph.2016.06.002, URL https://www.sciencedirect.com/science/article/pii/S0577907316301800.

Mero, J. L., 1960: Uses of the gamma-ray spectrometer in mineral exploration. *Geophysics*, **25 (5)**, 1054–1076, https://doi.org/10.1190/1.1438787.

Qwerty123uiop, 2013: Schematic view of a photomultiplier coupled to a scintillator, illustrating detection of gamma rays. Wikimedia Commons, URL https://commons.wikimedia.org/wiki/File:PhotoMultiplierTubeAndScintillator3.pdf, (PDF vector graphic), accessed 10/04/22.

Shirley, V. S., and C. M. Lederer, 1978: *Table of isotopes*. 7th ed., Wiley, New York.

UNSW School of Physics, n.d.: Gamma ray spectrometry. University of New South Wales, Sydney, (Student notes).

Virtanen, P., and Coauthors, 2020: SciPy 1.0: Fundamental Algorithms for Scientific Computing in Python. *Nature Methods*, **17**, 261–272, https://doi.org/10.1038/s41592-019-0686-2.

Zerby, C., A. Meyer, and R. Murray, 1961: Intrinsic line broadening in NaI(Tl) gamma-ray spectrometers. *Nuclear Instruments and Methods*, **12**, 115–123, https://doi.org/https://doi.org/10.1016/0029-554X(61)90119-7, URL https://www.sciencedirect.com/science/article/pii/0029554X61901197.